III Experimental Techniques

A wide range of experimental techniques were employed during the course of this research and their details are discussed herein.

III.I Photovoltaic and Electronic Device Fabrication

As discussed in Chapter 2, polymer fullerene bulk heterojunction solar cells consist of a planar, layered structure of thin films. In general, an indium tin oxide (ITO) coated glass substrate is etched to create the transparent anode. A layer of PEDOT:PSS is applied by spin coating, followed by the polymer:fullerene solution. Metallic cathodes are then evaporated under vacuum through a shadow mask in order to define the cathode. Finally, completed devices often undergo an annealing step in order to enhance the photovoltaic efficiency.

III.I.I Substrate cutting and ITO Patterning

Fabrication begins with a 50 x 75 x 1.1mm indium ITO coated boro-aluminosilicate glass sheet purchased from Delta Technologies.[1] The ITO coating is continuous and 140 nm thick,

with a sheet resistance of 10 Ω/□. The sheet is cut into rectangular photovoltaic substrates, 12 x 14mm using an automated, precision dicing saw equipped with a diamond resinoid blade. The ITO must then be etched to reveal the device anode; a 2mm wide strip that runs down the middle of the device (Figure 1). A Roland Stika cutting printer is used to prepare adhesive masks which are applied to the ITO film. The substrates are then submerged in an etchant solution consisting of water, hydrochloric acid and nitric acid in a ratio of 25:25:2. The substrates are etched at 50°C for 20 – 40 minutes (depending on the age of the etchant). The etched substrates are then sonicated in a 0.5% detergent solution for 10 minutes and deionised water for 10 minutes, both at 60°C. The substrates are then submerged for five minutes in a bath of HPLC grade acetone bath and then a bath of HPLC grade 2-propanol both at 50°C. After the solvent cleaning, the substrates are dried in a vacuum oven at 80°C over night before being submitted to a 6 second oxygen plasma etch in a Tegal Plasmod. The plasma raises the ITO work function[2] and removes residual organics from the surface, thereby improving its hydrophilicity.

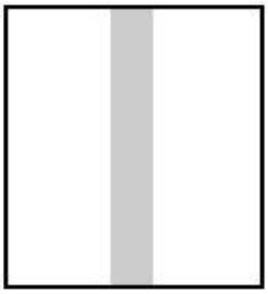

Figure 1. ITO pattern (grey) on glass substrate.

III.I.II Spin Coating of PEDOT:PSS and polymer:fullerene active layers

A layer of PEDOT:PSS, a conductive, transparent polymer, is then applied onto the ITO surface by spin coating. Spin-coating is a wet process for depositing thin films onto planar substrates. In general, a solution of the material to be deposited is applied to the substrate using a variable pipettor. The substrate is then spun, in the plane of the film, which causes the formation of a uniform thin film across the entire substrate surface. The layer thickness can be controlled by adjusting the spin speed, acceleration, the solvent, and the solution viscosity (via solution concentration and temperature). In all devices presented here, PEDOT:PSS was spin cast at 5000 rpm for 30 seconds, accelerating at 2500 rpm/s. Following deposition of the PEDOT:PSS the films are heat treated on a hot plate for 10 minutes at 140°C to remove residual moisture before being transferred to a moisture free nitrogen glovebox operating at 0 – 5 ppm O_2 and 1-2 ppm H_2O.

The photoactive polymer fullerene layer is then spin coated on top of the PEDOT:PSS. P3HT:fullerene solutions were prepared by creating a PCBM solution of known concentration and adding it to a known mass of P3HT in a glass vial inside the glovebox. The solvents used in this work include chlorobenzene and 1,2-dichlorobenzene (See Figure 2). Typical solution concentrations were 10 – 20 mg/mL P3HT. The solution was stirred overnight at ambient temperature to ensure the polymer was completely dissolved. Spin casting parameters were typically 600 – 1000 rpm for 30s – 1 minute with 200 rpm/s acceleration.

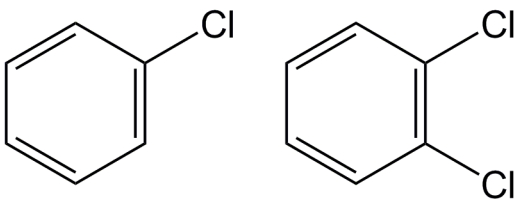

Figure 2. Chemical Structures of Chlorobenzene (left) and 1,2 dichlorobenzene (right)

Devices spin cast from chlorobenzene dried quickly and were subsequently placed in the bell-jar evaporator for cathode deposition within 10 minutes. Devices spin cast from di-chlorobenzene, on the other hand, dried more slowly due to the solvents higher boiling point. These devices were left in the glovebox overnight before being placed in the evaporator.

For fullerene-only devices, solution concentrations were higher (20 – 40 mg/mL) in order increase the solution viscosity and allow films of sufficient thickness to be spin cast.

III.I.III Cathode Deposition

The metallic cathode is deposited by thermal evaporation within a bell-jar evaporator inside the N_2 glovebox. Evaporation was initiated at a pressure of 5×10^{-7} torr after a 3 – 4 hr pump down on an oil diffusion pump. An evaporation mask was used to define the cathode dimensions. Three stripes were deposited on each device, perpendicular to the

ITO anode, as shown in Figure 3. This defined three separate solar cells, or pixels each with an area of 1.5mm x 2mm = 3mm^2.

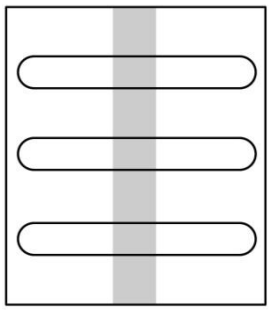

Figure 3. Device showing ITO stripe (grey) and Al cathode stripes.

Metal contacts were evaporated at a rate of 0.05 nm/s for the first 1nm, 0.1nm/s up until 10nm and at 1nm/s for the remainder of the layer. Typical aluminium contacts were 100 nm thick. The film thickness deposition rate was monitored using a calibrated Edwards FTM 5 quartz crystal growth monitor. Calibration was determined via DEKTAK surface profile measurements. Metals used for cathode deposition include Aluminium, Palladium and Silver.

For films that included an interfacial Lithium Fluoride (LiF) layer, LiF was evaporated from a second source before the metal, using a vertical shield to prevent cross contamination of the sources. LiF layers were typically 0.6nm thick, evaporated at a rate of 0.1nm/s. All metals and LiF were evaporated from tungsten boats. After the evaporation process was complete, the devices were left to cool for 10 minutes before the bell jar was vented

III.I.IV Thermal Annealing

Once the devices had been removed from the bell jar, most were submitted to a thermal annealing step on top of a digital hotplate within the glovebox. Devices were annealed at temperatures ranging from 110°C to 160°C for a duration of 1 – 30 minutes depending on the experiment.

III.II Photovoltaic Device Testing and Characterisation

Two techniques were used to test the photovoltaic performance of devices. Firstly, current-voltage measurements were obtained in the dark and under white light-illumination from a Newport 150W solar simulator. This measurement determines the white light efficiency of the solar cell as well as providing information about diode quality and parasitic resistances within the cell. Secondly, the external quantum efficiency (EQE) was measured, which measures the ratio of electrons generated per incident photon as a function of wavelength.

III.II.I Current Voltage Measurements

The white-light photovoltaic performance of a device was determined using a 150W Newport solar simulator, consisting of a 150W ozone free xenon arc lamp with an AM1.5G filter which produces a collimated 1.3” diameter beam. The device was placed at a distance from the lamp such that the incident power density was 100 mW/cm^2, measured using a Thorlabs digital optical power meter. The lamp spectrum is presented in Figure 4 and the

AM1.5G spectrum is included for comparison. The match between the two spectra is not perfect, but there is reasonably good agreement for wavelengths below 650nm, which is the absorption onset of the devices tested in this work. The Newport 150W solar simulator is a commonly used simulator within the field of polymer photovoltaics.

Although the lamp beam is collimated, it is not spatially uniform, as shown in Figure 5. The spatial variation was measured using the digital optical power meter with a mask to improve the measurement resolution. As shown, significant spatial variation exists, enough such that the three pixels on a single substrate experience significantly different light intensities if placed directly in front of the beam. This problem was overcome by using an x-y stage to ensure that each pixel was located in the same position for I-V measurements.

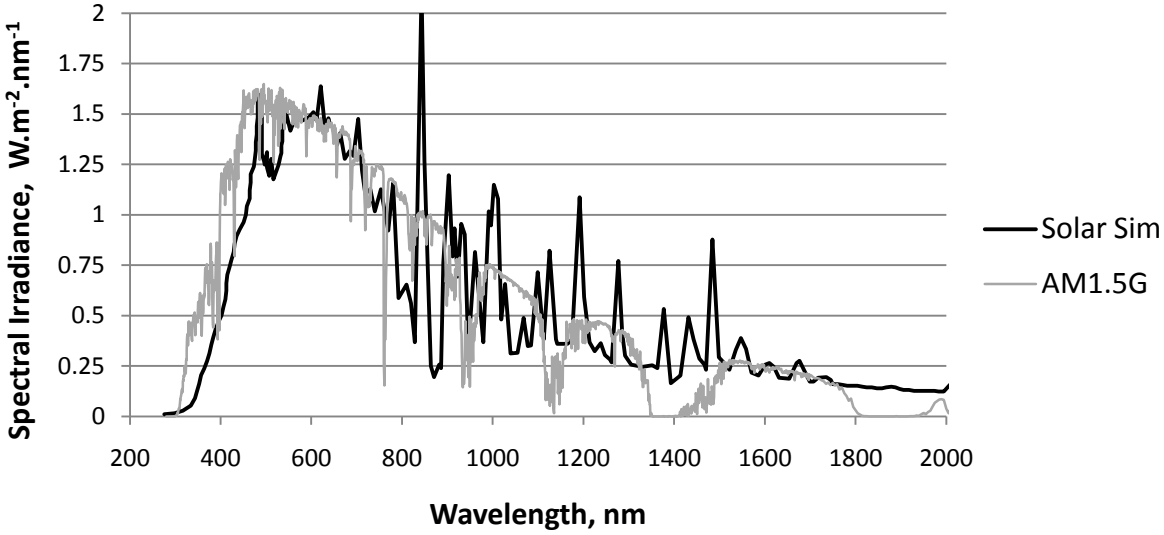

Figure 4. Comparison of the Newport 150W solar simulator spectrum with the ASTM G173-03 AM1.5 global spectrum, at 100mW/cm^2

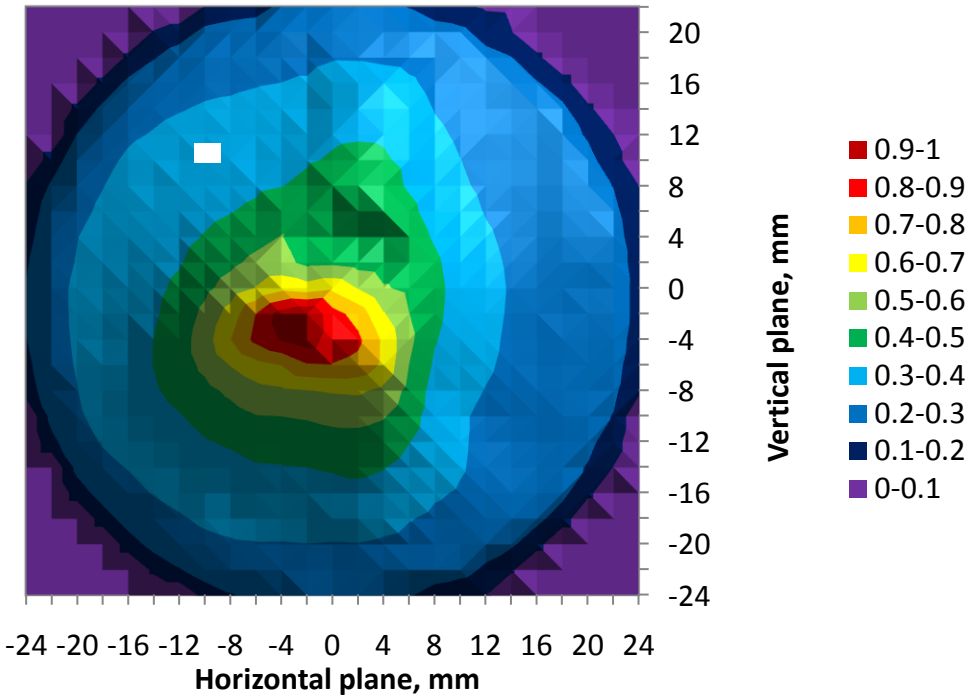

Figure 5. Normalised spatial power distribution of the Newport 150W solar simulator. The white rectangle represents the size and location of a single photovoltaic pixel.

The solar simulator mismatch factor was calculated according to published protocols.[3] The mismatch factor of a solar simulator can be calculated according to the equation:

$$M = \frac{\int_{\lambda_2}^{\lambda_2} E_{REF}(\lambda) S_R(\lambda) d\lambda}{\int_{\lambda_1}^{\lambda_2} E_{REF}(\lambda) S_T(\lambda) d\lambda} \frac{\int_{\lambda_1}^{\lambda_2} E_S(\lambda) S_T(\lambda) d\lambda}{\int_{\lambda_1}^{\lambda_2} E_S(\lambda) S_R(\lambda) d\lambda} \quad (1)$$

Where $E_{REF}(\lambda)$ is the normalised spectral irradiance of the reference spectrum (AM1.5G), $E_S(\lambda)$ is the normalised spectral irradiance of the solar simulator, $S_R(\lambda)$ is the normalised spectral responsivity of the reference cell, and $S_T(\lambda)$ is the normalised spectral responsivity

of the test cell. $E_S(\lambda)$ was obtained from NREL Renewable Resource Data Centre[4], $S_R(\lambda)$ was supplied by Newport. $S_R(\lambda)$ was supplied by Thorlabs for the digital optical power meter, while $S_T(\lambda)$ was determined using the lab's EQE set-up. Using this technique, mismatch factors of M = 0.95 to 0.97 were calculated, depending on the device under investigation.

Short circuit current densities under the reference spectrum were then calculated by dividing the measured short circuit current density by the mismatch factor. These are the values presented in the thesis as J_{SC}. Devices were tested under nitrogen atmosphere using a custom-built sample test cell containing a two-point electrical contact manifold.

A Keithley 2400 Source Measurement Unit (SMU) was used to apply a variable bias across the solar cell while simultaneously recording the current output. The result is an I-V curve (or J-V curve, where J = I divided by the device area), and Figure 6 presents J-V curves for a typical solar cell recorded in the dark and under illumination. Various parameters can be directly determined from the J-V curve and are indicated inFigure 6. The short circuit current, I_{SC}, refers to the current that is extracted from an illuminated solar cell when the bias across the device or circuit load, is zero. The open circuit voltage, V_{OC}, refers to the bias at which, the built in electric field within the solar cell is completely nullified and the extracted current is reduced to zero. At a certain point alon the J-V curve a maximum power density point is obtained.

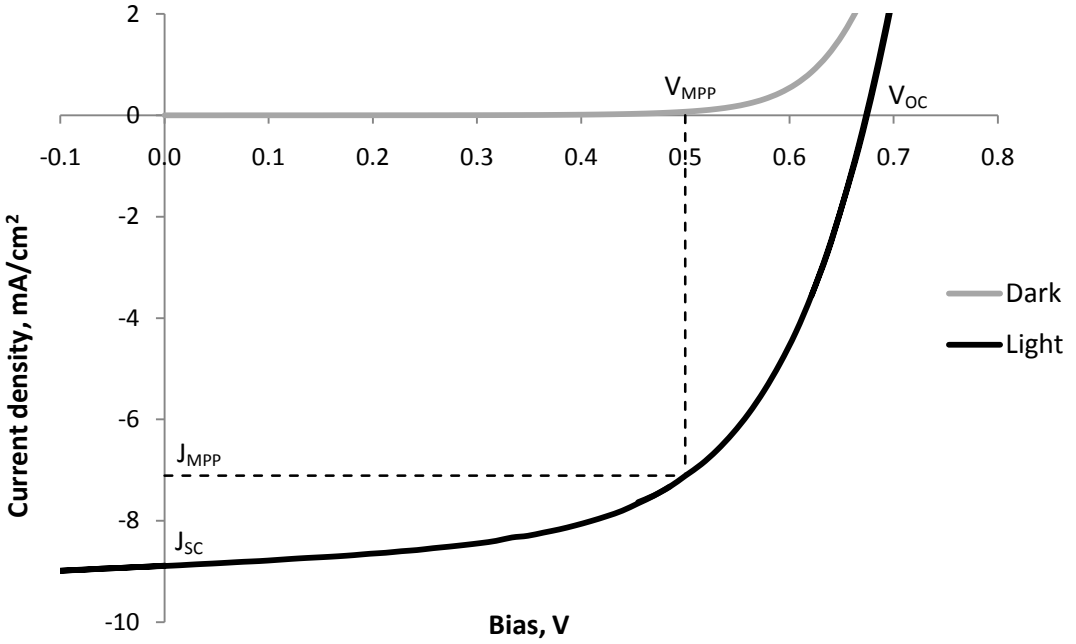

Figure 6. Typical J-V Curve

The fill factor represents the ratio of this maximum obtainable power density to the ideal maximum power density, J_{SC} x V_{OC}. Thus, the fill factor is calculated according to the equation:

$$FF = \frac{J_{MPP} \text{ x } V_{MPP}}{J_{SC} \text{ x } V_{OC}} \tag{2}$$

The solar cell efficiency, n, can then be calculated according to:

$$n = \frac{J_{MPP} \text{ x A x } V_{MPP}}{P_{IN}} \tag{3}$$

Where A is the device area and P_{IN} is the incident light power density

III.II.II Series and Shunt Resistance Calculations

The fill factor embodies the impact of parasitic series and shunt resistances on the I-V curve. Series resistance arises from the materials present in the device and from the interfaces between the different material layers[5]. The shunt resistance reflects the existence of alternative current pathways within the device, such as, micro-shorts and leakage currents around the device edges[5]. The values of the series and shunt resistances can be estimated using the I-V curve and the equivalent circuit model for solar cells incorporating parasitic resistance, shown in Equation 3.

$$I = -I_{SC} + I_0\left(e^{\frac{q(V+IR_S)}{kT}} - 1\right) + \frac{V + IR_S}{R_{SH}} \tag{4}$$

Where I is the measured current, I_0 is the reverse saturation current, q is the elementary charge, V is the applied voltage, R_S is the series resistance, k is Boltzmann's constant and R_{SH} is the shunt resistance. For the case where R_{SH} is large the second term can be neglected. By rearranging to make V the subject and differentiating with respect to I, Equation 4 is obtained:

$$\frac{dV}{dI} = -\frac{k_B T}{q}\left(\frac{1}{I_{SC} + I_0 - I}\right) - R_S \tag{5}$$

At open-circuit conditions, I = 0 and V = V_{OC}, giving

$$R_S = \frac{dV}{dI}\Big|_{V=V_{OC}} + \frac{k_B T}{q}\left(\frac{1}{I_{SC} + I_0}\right) \tag{6}$$

As the second term is small compared to the typical series resistance of these cells, R_S can be approximated by:

$$R_S \approx \left.\frac{dV}{dI}\right|_{V=V_{OC}} \tag{7}$$

To estimate R_{SH}, for cases where R_S is small we can neglect terms that contain R_S and directly differentiate Equation 3 with respect to V to give:

$$\frac{dI}{dV} = -\frac{q}{k_B T} I_0 e^{\frac{qV}{k_B T}} + \frac{1}{R_{SH}} \tag{8}$$

At short-circuit conditions, V = 0 and I = I_{SC}, giving:

$$\frac{1}{R_{SH}} = \frac{dI}{dV} - \frac{qI_0}{k_B T} \tag{9}$$

In the devices under consideration here, the second term on the right is negligible compared to dI/dV leaving:

$$R_{SH} \approx \left.\frac{dV}{dI}\right|_{V=0} \tag{10}$$

III.II.III External Quantum Efficiency (EQE) Measurements

In the context of photovoltaics, external quantum efficiency is defined as the percentage of incident photons that are converted to and extracted from the solar cell as photocurrent, as a function of the incident wavelength. This measurement can provide useful information about the solar cells effective wavelength range, the relative effectiveness of various

photoactive materials within the cell and can be used to check short circuit current values obtained from I-V measurements.

EQE measurements were carried out using the experimental set up presented in Figure 7. A xenon arc lamp was used as the light source coupled to a computer controlled Spectral Products CM110 dual grating monochromator in order to control the wavelength output. A 400nm cut-off filter was used to remove second order wavelengths. An iris determines the eventual spot size before the light is collimated and focused through two plano-convex lenses. A Keithley 2400 SMU measures the current produced by the solar cell and can also be used to apply a variable bias across the solar cell. The monochromator output is computer controlled and typically swept from 400nm to 800nm in 5nm increments.

Prior to the measurement of the test solar cell, a calibrated Newport 918-UV low-power photo-detector is used to determine the incident power at each the wavelengths of interest. This measurement is repeated after the test cell has been measured in order to ensure no changes in the lamps spectral output or intensity have occurred during the course of the experiment. The iris and lenses are calibrated to create a light spot with a diameter of 1 – 1.5 mm at the solar cell surface, so that the spot fits completely inside the pixel area of the device under examination. Minor variations in focal length due to chromatic aberration lead to incident flux variations of up to 30% at the solar cell surface.

EQE values were calculated assuming that the EQE is independent of the incident flux over the range of variation encountered

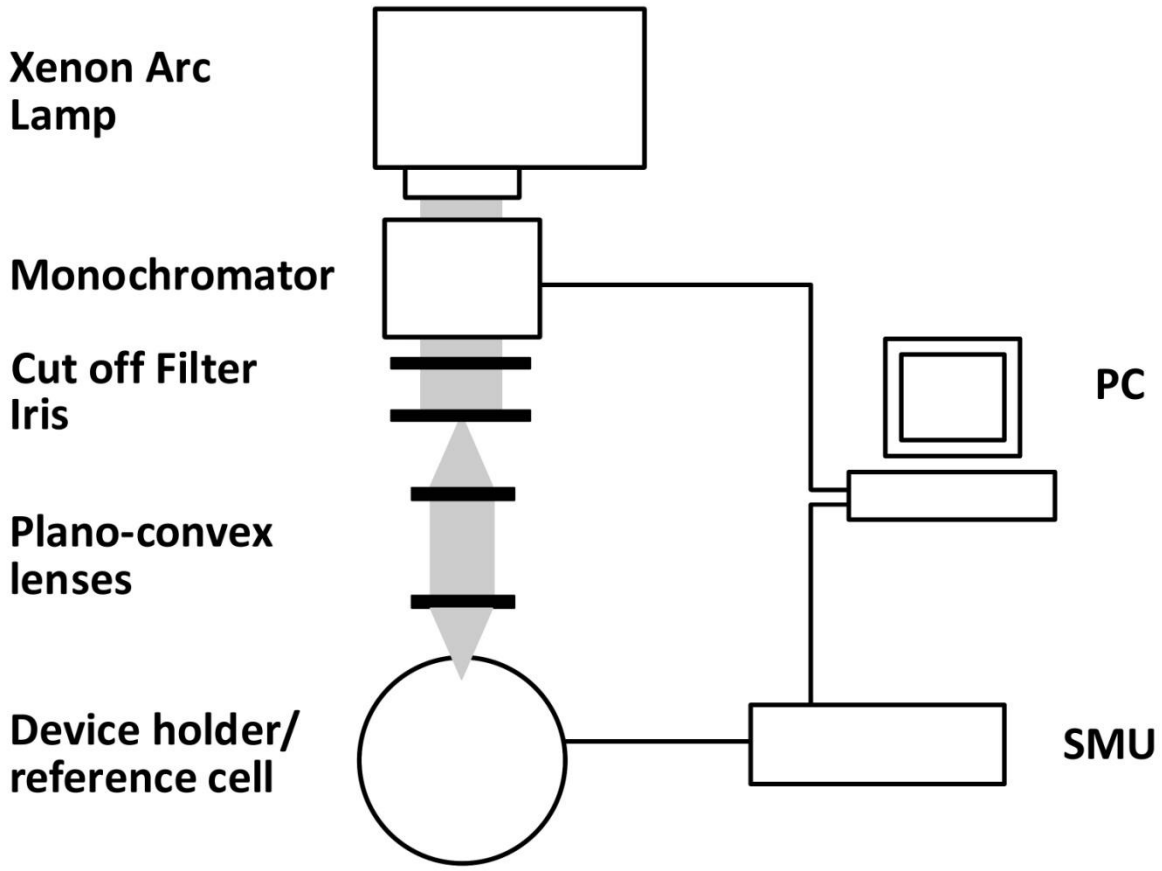

Figure 7. Schematic representation of the EQE measurement experimental setup

EQE was calculated according to the equation:

$$\mathrm{EQE}(\lambda) = \left(\mathrm{J_{SC,TEST}}\,(\lambda)\ \mathrm{x}\ 6.242\ \mathrm{x}\ 10^{18}\right)\ \mathrm{x}\ \left(\frac{\mathrm{S}(\lambda)_{\mathrm{REF}}\ \mathrm{x\ h\ x\ c}}{\mathrm{J_{SC,REF}}\,(\lambda)\ \mathrm{x}\ \lambda}\right)\ \mathrm{x}\ 100 \qquad (11)$$

Where the first term on the right relates to the electrons extracted from the solar cell and the second term on the right relates to the incident photon density. $J_{SC,TEST}(\lambda)$ is the current density output of the test cell at the given wavelength, 6.242×10^{18} is the number of

electrons per coulomb, $S(\lambda)_{REF}$ is the spectral responsivity of the Newport photo-detector in amps per watt, at the given wavelength, h is the Planck constant, c is the speed of light and $J_{SC,REF}(\lambda)$ is the current density output of the Newport photo detector for the given wavelength.

A typical EQE spectrum is presented in Figure 8. By numerically integrating the EQE spectra over the wavelength range of interest (Equation 11), an estimate of the short circuit current can be obtained that can then be compared to the value obtained from I-V measurements.

$$J_{SC} \approx \int_{\lambda_1}^{\lambda_2} EQE(\lambda) d\lambda \quad (12)$$

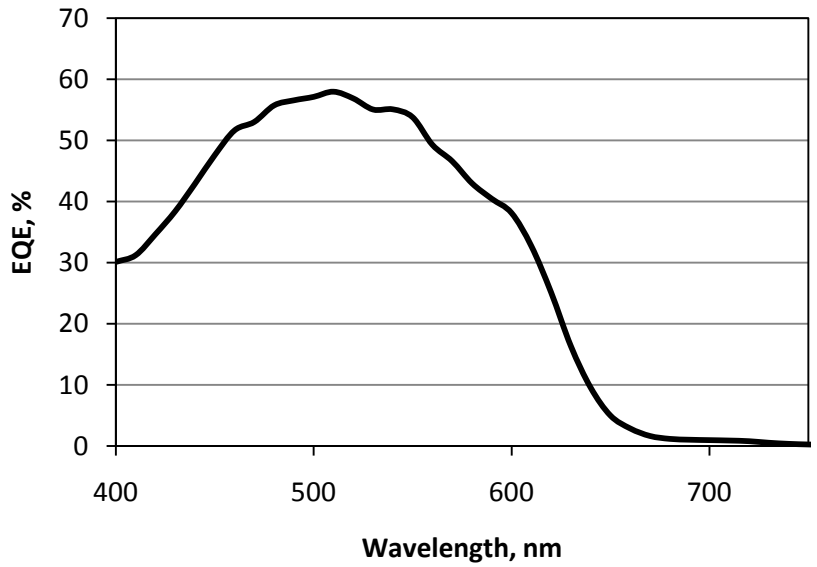

Figure 8. Typical EQE spectra

III.II.IV Temperature Dependent EQE Measurements

EQE measurements can also be conducted as a function of temperature through the use of an Oxford Instruments liquid nitrogen cryostat which allows measurements down to 77K. For an individual wavelength, a plot of the log of the short circuit current vs. the inverse of the temperature can be used to extract an activation energy, E_a, according to the equation

$$J_{SC} = J_0 e^{\frac{-E_a}{kT}} \tag{13}$$

The extracted activation energy relates to all thermally activated processes within the cell, and is mainly indicative of the quality of charge transport within the cell[6].

III.II.V Critical Field Modeling

The concept of the critical field was first introduced in 2008 by Marsh et al[7] who sought a simple, unifying model to explain the J-V curves of all the different types of excitonic solar cells. The authors identified germinate recombination as the primary loss mechanism in excitonic devices and the subsequent model they developed was based on a single fitted parameter, F_C, the critical field, which corresponds to the electric field required to split 50% of germinate charge pairs. The model is predicated on a version of the superposition approximation which states that the measured J-V response of a cell, $J(V)_T$ can be approximated by the sum of the photocurrent, $J(V)_{LIGHT}$, and dark current, $J(V)_{DARK}$. Rearranged, this implies that:

$$J_{LIGHT}(V) = J_T(V) - J_{DARK}(V) \tag{14}$$

Furthermore, due to a number of factors outlines in the paper, the authors assume that germinate recombination is the dominant loss mechanism in excitonic solar cells, leading to the statement:

$$J_{LIGHT}(V) = I \times e \times \eta(V) \tag{15}$$

Where I denotes the incident photon flux, e the elementary charge, and $\eta(V)$ is the quantum efficiency as a function of voltage. The authors define $\eta(F)$ as:

$$\eta(F) \propto \frac{k_s(F)}{k_s(F) + k_r(F)} \tag{16}$$

Where $k_s(F)$ is the rate of charge extraction as a function of the electric field within the device while $k_r(F)$ is the rate of charge recombination.

F, the electric field is defined as

$$F = \frac{V_0 - V}{d} \tag{17}$$

Where V_0 is the built in voltage across the device due to the difference between the anode and cathode work functions and is equal to the voltage at which J_{LIGHT} equals zero. d is the distance between the electrodes or in other words, the thickness of the active layer. The authors assume that recombination is independent of the electric field and extraction is highly field dependent and approximated by a first order Taylor expansion, as a result of which Equation 19 becomes:

$$\eta(F) \propto \frac{v_s F}{v_s F + v_r}$$

(18)

Where v_s and v_r are the characteristic rate constants of extraction and recombination of germinate pairs across the heterojunction respectively. The constant of proportionality in Equation 21 is equal to η_A x η_{ED}, where η_A is the light absorption efficiency at the given wavelength, and η_{ED} is the fraction of excitons that diffuse to a heterojunction and dissociate there to form a germinate charge pair. This product can be approximated by the devices external quantum efficiency under large reverse bias and can therefore be estimated from an I-V curve under monochromatic illumination. Dividing Equation 21 through by v_s then leads to:

$$\eta(F) = \eta_A x\, \eta_{ED} \left(\frac{F}{F + F_C}\right)$$

(19)

Where F_C is termed the critical field and is equal to v_r/v_s. As η_A x η_{ED}, d and V_0 can all be determined experimental data, F_C is left as the only variable and is determined by fitting Equation 22 to a monochromatic I-V curve, obtained using the EQE experimental set-up. Multiple wavelengths can be investigated in order to ascertain the dependence of F_C on the incident wavelength.

III.III Transmission Electron Microscopy

In Transmission Electron Microscopy (TEM) a thin sample is irradiated by a beam of primary electrons and an image is obtained from those electrons that are transmitted through the sample. TEM is capable of achieving resolutions several orders of magnitude greater than

optical microscopy due to the small de Broglie wavelength of electrons which makes it very useful for investigating features on the nanoscale. Since the exciton wavelength in polymer:fullerene solar cells is typically on the scale of 10 nm TEM provides the opportunity to directly investigate the polymer:fullerene morphology on this scale.

Figure 9 presents a schematic of a transmission electron microscope. Broadly speaking, electrons are emitted from an electron gun and illuminate the specimen through a two or three stage condenser lens system. Lenses in electron microscopy consist of rings of magnets, arranged to produce specific magnetic fields that can shape the electron beam as required. The objective lens, situated below the sample, determines the formation of the transmitted electron image or diffraction pattern of the sample. The objective aperture, located at the back focal plane, is inserted for bright field images but removed for diffraction imaging. For diffraction imaging an aperture is inserted at the first intermediate image. The transmitted electron distribution is then magnified through the intermediate lens, the strength of which can be varied, and the projector lens, which has a fixed strength, before being viewed on a fluorescent screen. The image can be recorded by direct exposure to photographic film or digitally with a CCD camera.

The TEM used to produce the images presented within this thesis is a JEOL-JEM 4000EX LaB_6 operating at 100 keV. Organic samples are relatively unstable under electron irradiation, with the threshold for electron knock-on damage in graphene defects

previously reported to be 80 keV.[8] For the work reported here, samples proved to be stable over the course of measurements at 100 keV. The trade off of operating at low voltages is that as the accelerating voltage is decreased the electron wavelength increases, according to the de Broglie relations. This leads to a reduction in imaging resolution.

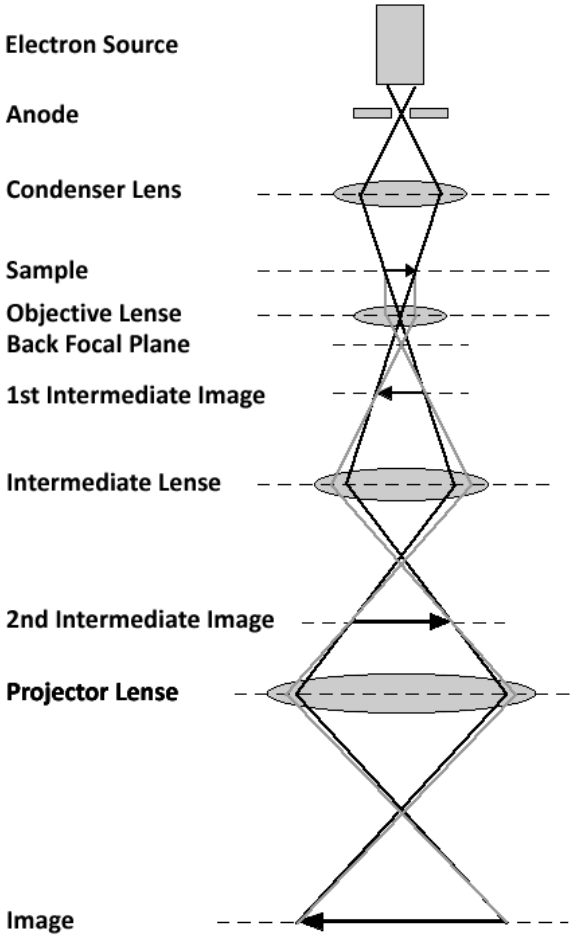

Figure 9. Ray Diagram of a Transmission Electron Microscope. Blue lines represent the imaged electron density. Image recreated from References [9] and [10].

The JEOL JEM 4000EX LaB6 has an internal closed loop heating system which allowed the direct observation of morphological changes during an annealing process. For this experiment, the heating system was ramped up to 150°C and then imaging was initiated.

The microscope calibration was verified using lead sulfide nanocrystals and compared with values from CaRIne Crystallography Software as shown in Figure 10.

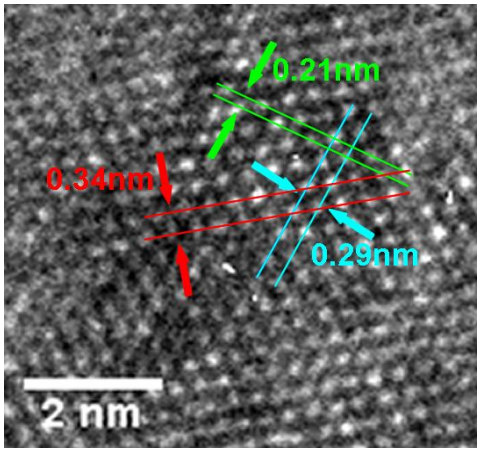

Plane	Measured, ± 0.01 nm	CaRine 3.1, nm
(111)	0.34	0.34
(200)	0.29	0.29
(220)	0.21	0.21

Figure 10. High resolution transmission electron micrograph of lead sulfide nanocrystals (left and measured lattice spacings and CaRine values.

III.III.II Sample Preparation

Another concern with working at low accelerating voltages is that the sample has to be extremely thin in order to ensure a sufficient number of electrons are transmitted in order to obtain an image. This requires samples that are thinner than a typical solar cell active layer. To accommodate this constraint, the following sample preparation methods were employed.

First, P3HT:PCBM solar cells were fabricated as previously described (see section II.I). Part of the active layer was then scraped off its substrate using a scalpel and sonicated in dichloromethane (a bad solvent for both PCBM and P3HT) for 3 minutes. The sonication was necessary in order to create particles with edges thin enough to allow high resolution TEM at low accelerating voltages. The resulting micron sized dispersion was then drop-cast onto lacey carbon copper grids. Samples were prepared from actual devices in order to insure the observed morphologies were truly characteristic. A sufficient number of flakes adhered to the TEM grid and overhung holes in the lacey carbon film to allow TEM analysis.

III.IV Space Charge Limited Current (SCLC) Mobility Measurements

The charge carrier mobilities of individual photovoltaic materials and blended films are of significant interest as they directly determine the drift velocities of separated charge carriers in devices according to the equation:

$$v_d = \mu E \tag{20}$$

Where v_d is the drift velocity, μ is the charge mobility and E is the applied electric field. Mobilities can be determined via a number of experimental techniques including field effect transistor measurements, time of flight measurements and space charge limited current measurements. Of these methods, the SCLC measurement has emerged as the most popular technique for organic photovoltaics due to its simplicity and to the fact that the sample architecture that closely mimics an actual photovoltaic device.

III.IV.I Space Charge Limited Current Mobility Theory

Space charge limited current refers to the phenomenon whereby the flow of current through a device is limited by a build-up of charge on the device side of the charge injecting cathode, due to the large disparity in charge carrier mobilities on either side of the electrode/device interface.

In such a case, the current density can be modeled by the Mott-Gurney Law:[11]

$$J = \frac{9}{8}\mu_0 \epsilon \epsilon_0 \frac{V^2}{L^3} \tag{21}$$

Where μ_0 is the zero field free carrier mobility ε the relative static permittivity of the material, ε_0 the permittivity of free space, V the applied voltage, and L the distance between the electrodes. Equation 13 is based on the assumptions that there is only one type of charge carrier present, that the mobility is independent of the applied electric field and that the material is free of trapping effects. Careful selection of electrode materials can ensure the first condition is met. Charge carrier mobilities in fullerene derivatives generally exhibit very little field dependence if the applied bias is low (less than 3V);[12] however this is not necessarily true for other organic semiconductors. To account for this, and the existence of trap states in these materials a modified Mott-Gurney law is appropriate[11]:

$$J = \frac{9}{8}\mu_0 \epsilon \epsilon_0 \frac{V^2}{L^3} \theta_0 \exp\left\{\frac{0.891}{kT}\left(\frac{e^3 V}{\pi \epsilon \epsilon_0 L}\right)^{1/2}\right\} \tag{22}$$

Where:

$$\theta_0 = \frac{N_c}{N_t} \exp\left(-\frac{A}{kT}\right) \quad (23)$$

θ_0 represents the proportion of free charge carriers. N_c is the effective density of states in the conduction band and N_t is the density of traps. A represents the average trap depth, k is the Boltzmann constant, T is temperature and e is the elemental charge. For the experiments conducted herein, in order to simplify the calculations, θ_0 was set to one, meaning that the mobility values reported herein represent a lower limit of the actual value.

III.IV.II Sample Preparation

Sample preparation is similar to the fabrication of photovoltaic devices. To measure the electron mobility of fullerene derivatives, thin films of the fullerene derivative were spin cast from chlorobenzene onto PEDOT:PSS coated ITO glass substrates. A typical fullerene solution concentration was 25 mg/mL resulting in a film with a thickness of approximately 100nm. The metal electrode consisted of a thermally evaporated 1 nm thick layer of lithium fluoride, followed by 70nm of aluminium. The LiF conduction band is expected to pin to the fullerene LUMO, providing an ohmic contact for the injection of electrons. At the anode, the work function of PEDOT:PSS is significantly higher than the fullerene HOMO, preventing the injection of holes.

To measure the hole mobility of polymer/fullerene blended films, palladium was used as a cathode. The high 5.12 eV work function of Palladium creates a large mismatch with the fullerene LUMO, preventing the injection of electrons, while at the anode, PEDOT:PSS makes an ohmic contact with the polymer HOMO for the injection of holes.

III.IV.III Experiment and Calculation

For SCLC measurements, J-V curves were taken in the dark out to a forward bias of 4V. Equation 20 was then fitted to the resulting J-V curve by adjusting the zero field mobility, μ_0. ε_r was taken to be 3.9.[13] L, the film thickness was determined using a DEKTAK profilometer. Equation 21 was also fitted to the I-V curve in order to check for any field dependency. In all cases, films of two different thicknesses were tested, in order to ensure that the SCLC effect was dependent on the film of interest.

III.V Atomic Force Microscopy (AFM)

Atomic force microscopy involves rastering a cantilever with an ultra fine tip across the surface of a sample. Interactions between the cantilever tip and the sample lead to deflections of the tip according to Hooke's law. This deflection is measured by a laser beam reflected off the top surface of the cantilever tip and detected by a photodiode array. Piezoelectric motors are used to precisely control the movement of the cantilever and/or the sample in the x, y and z directions.

Broadly speaking, AFMs can be operated in either static or dynamic modes. In static mode, the cantilever tip is not vibrating and the tip is manipulated in the z direction in order to maintain a constant force between tip and sample while being scanned through x and y. Static, or contact mode AFM can result in damage to the surface of soft samples, such as the organic thin films.

To avoid such damage, dynamic mode AFM is often used and is characterized by the driven oscillation of the cantilever tip at, or close to, its fundamental resonant frequency. The oscillation amplitude, phase and frequency are affected by tip-sample interactions and changes relative to the reference oscillator provide information about the sample. Non-contact AFM is a type of dynamic mode AFM whereby the cantilever is oscillated at an amplitude of less than 10nm, allowing it to be influenced by van der Waals forces from the sample. The tip height is varied to maintain a constant frequency or amplitude of oscillation with the requisite alterations in z-value providing a topographical image of the sample surface.

For the work conducted herein, a Park Scientific Instruments CP-II AFM in non-contact mode was used with CSC38/AlBS tips from MikroMasch. Images were taken over areas of 4

– 100 μm^2. Gain values varied between 0.08 and 1.00 with offset values varying between -0.055 to -0.076

The data matrix provided by an AFM scan can be processed to produce a 2D or 3D image. In addition, it can be used to determine average roughness values for the scanned area. Numerous equations exist for the determination of roughness, and herein, root mean squared (RMS) roughness values have been utilized, calculated by WSxM software according to the equation

$$R_q = \sqrt{\frac{1}{N^2}\sum_{x=1}^{n}\sum_{y=1}^{n}(Z(x,y) - \bar{Z})^2} \quad (24)$$

Where n is the total number of data points, x and y are the pixel locations, Z(x,y) is the z-value for pixel location x,y and Z bar is the mean z value for the entire array.

III.VI Contact Profilometry Measurements of Film Thickness

Although AFM can provide exceptional vertical resolution, and can be used to determine film thicknesses, it is a relatively time consuming technique and not particularly suitable or necessary for this routine measurement. Instead, a Veeco DEKTAK surface profiler was employed. A diamond tipped stylus is scanned across the sample surface in a single line, with a given contact force. Vertical movements of the tip across the surface are translated

into changes in inductance within an electrical circuit, and presented as a 2D plot of the sample surface.

By scanning across the width of a metal cathode on a solar cell, the electrode thickness can be measured, with an accuracy of less than 1nm. The thickness determined by DEKTAK measurement can then be used to calibrate the crystal thickness monitor in the evaporation bell jar.

For measuring the thickness of polymer layers, a step is made by scratching off a portion the film with a scalpel or cotton tip. The step height can then be measured, revealing the film thickness. For films containing more than one layer, such as a PEDOT:PSS/polymer:fullerene stack, the thickness of a stand-alone PEDOT:PSS film is measured first. The thickness of the two-film stack is then measured, with the difference between the two measurements taken to be the thickness of the polymer fullerene layer. Sometimes, due to the scratching method used to make the step and the various adhesion forces at the layer interfaces, it is possible to see two step heights within a single scan, allowing for direct verification of the polymer:fullerene film thickness.

III.VII Optical Surface Profilometry by MicroXAM

An AFM provides superb resolution for examining surface topography, but is limited to areas below 100 x 100nm. For larger scale investigations, a MicroXAM 5000 3D surface profiler was used. The MicroXAM 5000 uses optical interferometry to measure vertical features from less than one nanometer to several millimeters in height. A schematic is presented in Figure 11. A single light source is split into two identical beams, only one of which is incident on and reflected from the sample. The reflected sample beam is then recombined with the second, reference beam before arriving at a detector. Any differences in the beam paths, due to differences in the path length, or changes in refractive index along the path, will lead to a slight phase difference between the two beams and interference effects upon recombination. This interference pattern is interpreted by the MicroXAM software to produce 3D surface maps and a range of topographical parameters including surface roughness.

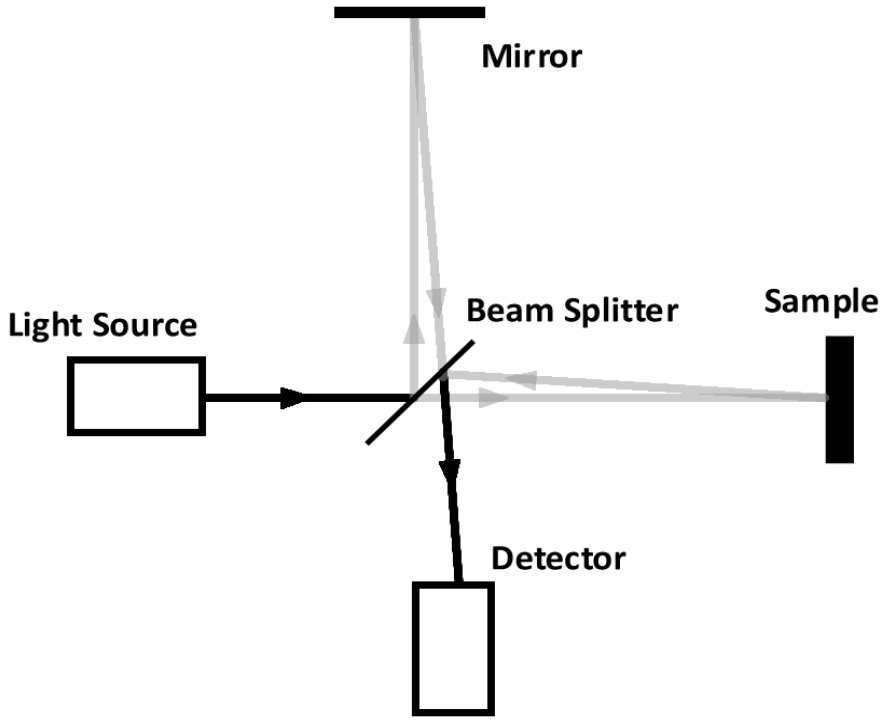

Figure 11. Optical Inteferometry set-up

III.VIII Calculation of Sheet Resistance

Sheet resistance was calculated for thin films of glycerol doped PEDOT:PSS using a custom built four point probe system. A four point probe system was used in order to remove the effects of contact resistance from the measurements. The experimental set-up is represented in Figure 12.

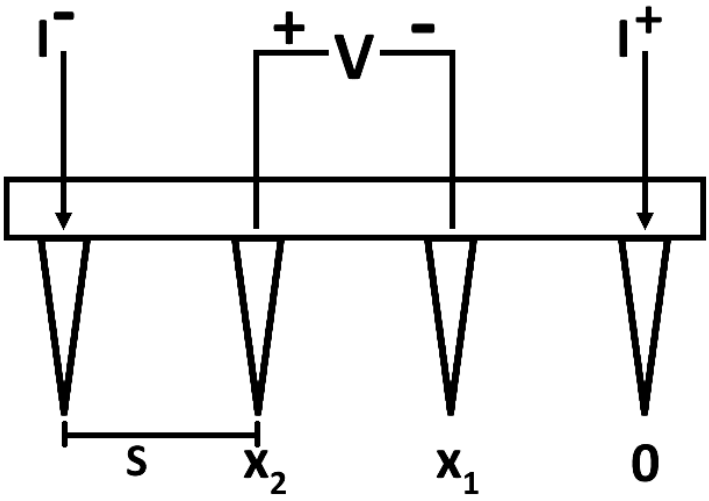

Figure 12. Four point probe arrangement for sheet resistance calculations

In general, resistance within a conductor can be described by:

$$\Delta R = \rho\left(\frac{dx}{A}\right) \tag{25}$$

where ρ is the resistivity, A is the cross sectional area and L is the length. In a four point system of the type shown in Figure 12, one can imagine current rings emanating from the outermost probe tips. Assuming that the probe tips are infinitesimal and that the sample is semi-infinite in the lateral dimension, for a thin sheet with sample thickness, t, the area that these rings occupies can be described by:

$$A = 2\pi xt \tag{26}$$

Substituting Equation 24 into 23 and integrating gives:

$$R = \int_{x1}^{x_2} \rho \frac{dx}{2\pi xt} = \int_{s}^{2s} \frac{\rho}{2\pi t}\frac{dx}{x} = \frac{\rho}{2\pi t}\ln(x)\Big|_{s}^{2s}$$

(27)

Due to the superposition of current at the outer two tips R = V/2I, giving:[14]

$$\rho = \frac{\pi}{\ln(2)} t \left(\frac{V}{I}\right)$$

(28)

Which stands true for a semi-infinite sheet with a very thin sample thickness (t << s). To account for a non-infinite sheet finite size correction factors must be included, such that:

$$\rho = \frac{\pi}{\ln(2)} t \left(\frac{V}{I}\right) f_1 f_2$$

(29)

Where f_1 is the finite thickness correction and f_2 is the finite width correction. For a sample with an insulating bottom boundary (as in the current case):

$$f_1 = \frac{\ln(2)}{\ln\left[\frac{\sinh(t/s)}{\sinh(t/2s)}\right]}$$

(30)

The modified PEDOT:PSS layer is approximately 50 nm thick while the probe separation, s, is 1.5 mm. In such a case f_1 tends towards unity. Regarding f_2, for a square sample of side length d = 10mm, d/s = 6.7, and f_2 = 0.83 according to the Figure 13 below:[15]

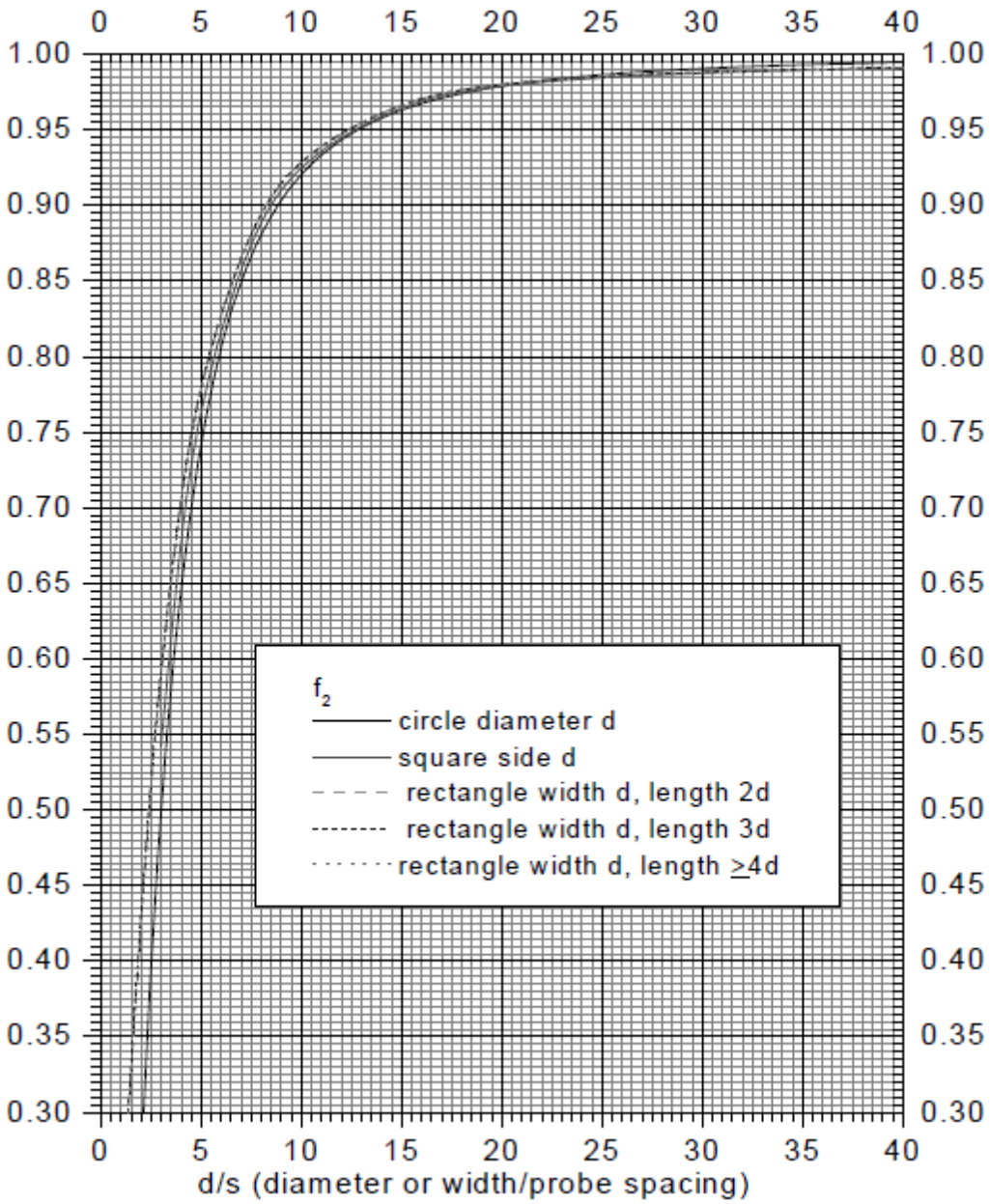

Figure 13. Chart for determining the finite width correction factor for four point probe resistivity measurements. Original source: F.M. Smits, "Measurement of Sheet Resistivities with the Four-Point Probe", The Bell System Technical Journal, 37, 711-718 (1958).

Taking into account the correction factors, the resulting equation is:

$$\rho = 0.83t\frac{\pi}{\ln(2)}\left(\frac{V}{I}\right) \quad (31)$$

Sheet resistance, R_s, is defined as p/t giving:

$$\frac{\rho}{t} = R_s = \frac{0.83\pi}{\ln(2)}\left(\frac{V}{I}\right) = k\left(\frac{V}{I}\right) \quad (32)$$

k = 3.76, and was used herein as the k value for calculations of the sheet resistance of PEDOT:PSS and modified PEDOT:PSS films. By plotting current versus voltage for samples in the four point set-up, a straight line is obtained, the gradient of which is employed in Equation 26 to obtain the sheet resistance.

III.IX Cyclic Voltammetry

In cyclic voltammetry, a dissolved species of interest, in this case a fullerene derivative, is electrolysed (oxidised or reduced) via the application of a triangular voltage waveform within a three electrode system. Voltage is measured between the working and reference electrodes while current is measured between the working and auxiliary electrodes.

Application of a voltage to the working electrode raises the Fermi level to a point where it is thermodynamically favorable for an electron to be injected into the fullerene LUMO. Whether the process then occurs is dependent on the kinetics of the electron transfer.

Considering a single electron transfer reaction between two species (O) and (R):

$$O_{(S)} + e^- \underset{k_{ox}}{\overset{k_{red}}{\rightleftharpoons}} R_{(S)}$$

(33)

The current flowing in either the reductive or oxidative direction can be predicted using the following equations:

$$i_a = -FAk_{ox}[R]_0$$

(34)

$$i_c = -FAk_{red}[O]_0$$

(35)

Where F is Faraday's constant, A the electrode area, k the rate constant for electron transfer and $[R]_0$ and $[O]_0$ the concentration of the species at the electrode surface. Analysis of the effect of the applied voltage on the reaction rate constants reveals an exponential relationship according to:[16]

$$k_{red} = Z\exp\left\{\left(\frac{-\Delta G_{red,V=0}}{RT}\right)\left(\frac{-\alpha FV}{RT}\right)\right\}$$

$$k_{ox} = Z\exp\left\{\left(\frac{-G_{ox,V=0}}{RT}\right)\left(\frac{(1-\alpha)FV}{RT}\right)\right\}$$

(36)

Where Z is a constant, $\Delta G_{red,V=0}$ and $\Delta G_{ox,V=0}$ are the activation energies for the reduction and oxidation reactions at zero applied bias, R is the Boltzmann constant, T is temperature, α is the transfer coefficient and V is the applied bias. This shows that as the bias is ramped up, the electron transfer rate, and therefore for the measured current, increases exponentially. However, this trend obviously cannot continue indefinitely and an investigation of Equation 29 and 30 suggest that the reactant concentration at the

electrode surface may have a limiting effect. If the reaction rate constant (k_{ox} or k_{red}) is large, the current will be controlled by the rate at which fresh reactant diffuses to the electrode surface from the bulk solution. The diffusion rate is controlled by the concentration gradient which is initially high as the distance between the electrode surface and the bulk concentration is very small. Over time, the diffusion rate drops as a greater volume of solution is depleted of reactant and the distance between the electrode surface and the bulk concentration increases.

The characteristic peaks observed in cyclic voltammograms occur because at some point the diffusion layer grows sufficiently large such that the flux of reactant to the electrode surface is no longer sufficient to maintain the reaction rate and the current begins to drop off. For a current that is 'diffusion controlled', the drop off in current density can be modeled by the Cottrell equation:[16]

$$i = \frac{nFAC_0\sqrt{D}}{\sqrt{\pi t}} \qquad (37)$$

Where I is the current, n is the number of electrons to reduce/oxidise one molecule of analyte, F is Faraday's constant, A is the electrode area, C_0 is the concentration of the reactant in the bulk solution, D is the diffusion constant, t is time.

For the work conducted herein, C-V measurements were conducted using an Ivium CompactStat potentiometer. Fullerene derivatives were dissolved in a 4:1 solvent mixture of 1,2-dichlorobenzene and anhydrous acetonitrile with 0.1M of $Bu_4N(PF_6)$ as the dissolved electrolyte. Fullerene concentrations were typically 0.1 mg/mL. A glassy carbon working electrode, platinum mesh counter electrode and a non-aqueous Ag/Ag^+ reference electrode were used.

Cyclic voltammetry has been used in this work primarily to determine the LUMO level of fullerene moieties. The lowest unoccupied molecular orbital corresponds to the energy level of the first electron added during the first reduction reaction of a C-V experiment. As a result, relative differences in LUMO levels can be determined from the mid-point of the first reduction couple on a voltammogram, as shown in Figure 14. The redox potentials are determined relative to the half-cell potential of the reference electrode, in this case Ag/Ag+. As the half-cell potential of the reference electrode can drift over time and is influenced by the surrounding solution, it is common practice to present all CV results relative to an internal standard such as ferrocene. This is done by adding a small amount of ferrocene to the fullerene solution after the C-V measurement has been taken before repeating the measurement, in order to reveal the Ferrocene peak. Although it is possible to then convert fullerene potentials versus Ferrocene to another reference such as the standard hydrogen electrode or absolute vacuum,[17] this introduces significant errors into the measurement.[18,19] In acetonitrile at 25°C:

Fc/Fc^+ is +0.40V versus SCE,

SCE is +0.242V versus NHE

NHE is 4.6 ± 0.1V from vacuum

Therefore, assuming that 4:1 acetonitrile:dichlorobenzene + 0.1MBu_4NBF can be considered equivalent to acetonitrile and that there is very little difference between room temperature and 25°C, one could take the fullerene redox potential measured in this system, subtract the mid-point potential for Fc/Fc^+ then add 5.24 V to it, to give a value relative to vacuum. However, the errors introduced (at least 0.14V) are on the order of expected differences between the fullerene and would render the results meaningless. Thankfully, such an approach is not necessary in order to determine relative differences between fullerene species. As such, all electrochemical potentials are presented relative to the internal Ferrocene standard.

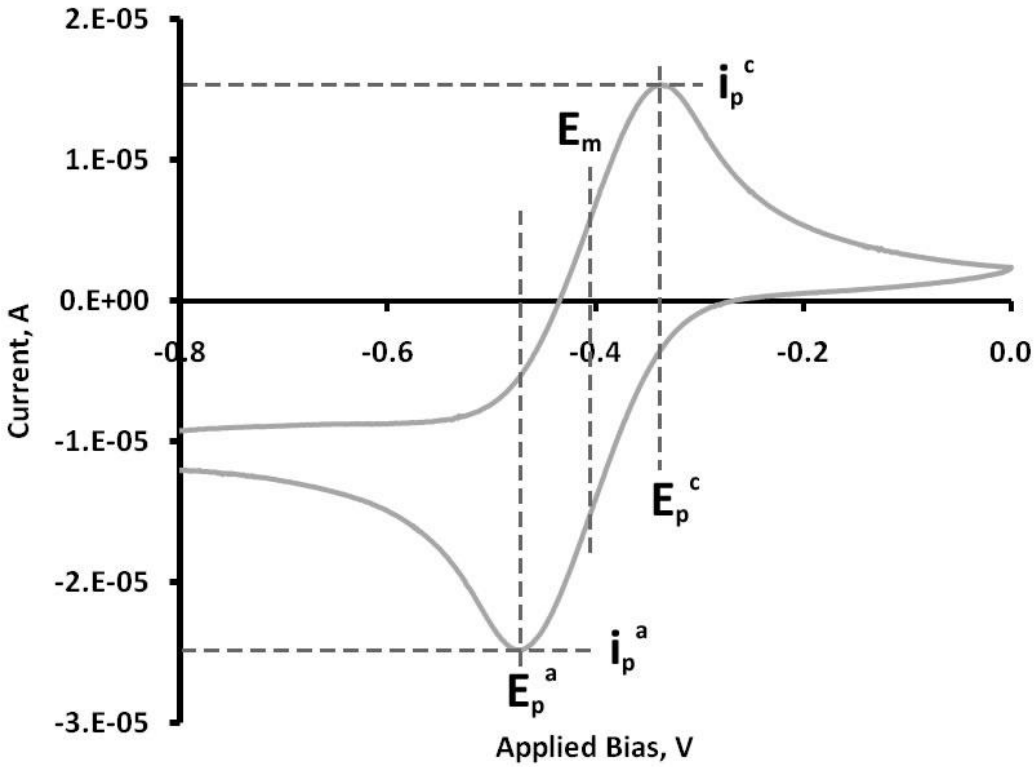

Figure 14. Typical Voltammogram showing one redox couple. I_p^a is the peak reduction current, E_p^a is the reduction peak potential, i_p^c is the peak oxidation current, E_p^c is the oxidation peak potential and E_m is the redox couple mid-point potential.

III.X UV/Visble Absorption Spectrum

The absorbance of a thin film as a function of the wavelength of the incident light can provide valuable information about chemicals present in the film and about the band gap energies of organic semiconductors. The UV-Vis spectra presented in this thesis were measured using a Cary 5000 UV-visible-NIR spectrometer. For UV-vis measurements, light from the tungsten-halogen or deuterium sources passes through the monochromator and is then split into two beams, one of which passes through the sample under investigation, and the other through a reference sample, before hitting separate silicon photodiode detectors. The difference in the light intensity arriving at the two detectors reveals the absorption of the sample at the incident wavelength. For thin film samples, preparation involved spin coating a solution onto ITO coated glass. An ITO coated glass substrate was used as the reference.

III.XII References

[1] Kim, Y. *et al.* A strong regioregularity effect in self-organizing conjugated polymer films and high-efficiency polythiophene: fullerene solar cells. *Nature Materials* **5**, 197-203 (2006).

[2] Hill, I. G., Milliron, D., Schwartz, J. & Kahn, A. Organic semiconductor interfaces: electronic structure and transport properties. *Applied Surface Science* **166**, 354-362 (2000).

[3] Shrotriya, V. *et al.* Accurate Measurement and Characterization of Organic Solar Cells. *Advanced Functional Materials* **16**, 2016-2023 (2006).

[4] *Reference Solar Spectral Irradiance: Air Mass 1.5*, <http://rredc.nrel.gov/solar/spectra/am1.5/> (

[5] Nelson, J. *The Physics of Solar Cells*. (2003).

[6] Kyungkon, K., Jiwen, L., Namboothiry, A. G. & Carroll, D. L. Roles of donor and accepto nanodomains in 6% efficient thermally annealed polymer photovoltaics. *Applied Physics Letters* **90** (2007).

[7] Marsh, R. A., McNeill, C. R., Abrusci, A., Campbell, A. R. & Friend, R. H. A Unified Description of Currentâ€"Voltage Characteristics in Organic and Hybrid Photovoltaics under Low Light Intensity. *Nano Letters* **8**, 1393-1398, doi:10.1021/nl080200p (2008).

[8] Warner, J. H. *et al.* Structural transformations in graphene studied with high spatial and temporal resolution. *Nat Nano* **4**, 500-504 (2009).

[9] Goodhew, P. *Transmission Electron Microscopy*, <http://www.matter.org.uk/tem/default.htm> (2000).

[10] *Transmisison Electron Microscopy*, <http://www.mete.metu.edu.tr/pages/tem/TEMtext/TEMtext.html> (

[11] Murgatroyd, P. Theory of space-charge limited current enhanced by Frenkel effect. *J. Phys. D* **3** (1970).

[12] Lenes, M. *et al.* Electron Trapping in Higher Adduct Fullerene-Based Solar Cells. *Advanced Functional Materials* **19**, 3002-3007 (2009).

[13] Popescu, L. M., Hof, P. v. t., Sieval, A. B., Jonkman, H. T. & Hummelen, J. C. Thienyl analog of 1-(3-methoxycarbonyl)propyl-1-phenyl-[6,6]-methanofullerene for bulk heterojunction photovoltaic devices in combination with polythiophenes. *Applied Physics Letters* **89**, 213507 (2006).

[14] Schroeder, D. K. *Semiconductor Materials and Device Characterization*. (Wiley, 1990).

[15] Smits, F. M. Measurement of Sheet Resistivities with the Four-Point Probe. *The Bell systems Technical Journal* **37**, 711-718 (1958).

[16] Bard, A. J. & Faulkner, L. *Electrochemical Methods: Fundamentals and Applications, 2nd Edition*. (Wiley, 2001).

[17] Cernini, R. *et al.* Electrochemical and optical studies of PPV derivatives and poly(aromatic oxadiazoles). *Synthetic Metals* **84**, 359-360 (1997).

[18] Connelly, N. G. & Geiger, W. E. Chemical Redox Agents for Organometallic Chemistry. *Chemical Reviews* **96**, 877-910, doi:10.1021/cr940053x (1996).

[19] Trasatti, S. The absolute electrode potential: An explanatory note. *Pure and Applied Chemistry* **58**, 955-966 (1986).